

In-situ x-ray phase contrast observation of the full penetration spot welding on limited aluminum material thickness

Cite as: J. Laser Appl. **34**, 042019 (2022); <https://doi.org/10.2351/7.0000772>

Submitted: 23 June 2022 • Accepted: 13 September 2022 • Published Online: 17 October 2022

 Woo-Sik Chung, André Häusler, Marc Hummel, et al.

COLLECTIONS

Paper published as part of the special topic on [Proceedings of the International Congress of Applications of Lasers & Electro-Optics \(ICALEO 2022\)](#)



View Online



Export Citation



CrossMark

ARTICLES YOU MAY BE INTERESTED IN

[Evaluation of narrowed weld pool shapes and their effect on resulting potential defects during deep penetration laser beam welding](#)

Journal of Laser Applications **34**, 042005 (2022); <https://doi.org/10.2351/7.0000733>

[Application of adjustable ring mode laser in remote laser welding of additive manufactured AlSi10Mg alloy](#)

Journal of Laser Applications **34**, 042007 (2022); <https://doi.org/10.2351/7.0000794>

[Sustainable laser metal deposition of aluminum alloys for the automotive industry](#)

Journal of Laser Applications **34**, 042004 (2022); <https://doi.org/10.2351/7.0000741>



**Journal of
Laser Applications**







LEARN MORE

Why publish with us?


In-situ x-ray phase contrast observation of the full penetration spot welding on limited aluminum material thickness

Cite as: J. Laser Appl. 34, 042019 (2022); doi: 10.2351/7.0000772

Submitted: 23 June 2022 · Accepted: 13 September 2022 ·

Published Online: 17 October 2022



Woo-Sik Chung,¹  André Häusler,¹ Marc Hummel,² Alexander Olowinsky,¹  Arnold Gillner,^{1,2} Felix Beckmann,³ and Julian Moosmann³

AFFILIATIONS

¹Fraunhofer Institute for Laser Technology ILT, Steinbachstr. 15, Aachen, North Rhine-Westphalia 52074, Germany

²Chair of Laser Technology LLT, Steinbachstr. 15, Aachen, North Rhine-Westphalia 52074, Germany

³Institute of Materials Physics, Helmholtz-Zentrum HEREON, Notkestr. 85, Hamburg 22607, Germany

Note: Paper published as part of the special topic on Proceedings of the International Congress of Applications of Lasers & Electro-Optics 2022.

ABSTRACT

The laser-spot welding process of aluminum alloy 1050A with a limited thickness is observed with the x-ray phase contrast method to investigate the melt dynamic especially when the melt penetrates the material. The laser-spot welding is investigated with two different wavelengths of the laser beam source: 515 and 1030 nm to investigate the influence of the absorptivity. The melt progressively penetrates the material during the spot-welding process until reaching the bottom side of the material and when the melt penetrates the lower side of the material, the so-called “lens-like” melt appears at the lower side due to the surface tension. At a comparable beam intensity value, the oscillation of the “lens-like” melt at the lower side of the material is driven by the expansion of vapor capillary. This expansion occurs inside of the material and directly above the “lens-like” melt. The shape of the expanded vapor determines the volume as well as the geometry of the resulting melt volume. Furthermore, the transition from the heat conduction welding mode to the keyhole welding mode is investigated by defocusing the laser beam for the beam source with a 515 nm wavelength. At a given variation, a clear difference between either mode is observed with the x-ray phase contrast method.

Key words: x-ray phase contrast observation, laser spot welding, vapor capillary evolution, melt dynamic, melt solidification

© 2022 Author(s). All article content, except where otherwise noted, is licensed under a Creative Commons Attribution (CC BY) license (<http://creativecommons.org/licenses/by/4.0/>). <https://doi.org/10.2351/7.0000772>

I. INTRODUCTION

The welding of limited material thickness in the overlap configuration grows its importance over time due to its application for the battery interconnection, especially for the cylindrical cells.^{1,2} As the material thickness is limited, the uncontrolled penetration of the laser beam during the welding process will evoke melt ejection on the back side of the material. This melt ejection will lead to the melt volume loss and resulting spatters, which could impact undesired side effects to the battery cells.

In terms of the laser-spot welding process, the full penetration of the single aluminum alloy 1050A with a thickness of 0.5 mm is

investigated with heat conduction and keyhole welding (KW) mode by applying two different laser beam sources. The applied laser beam wavelengths are 515 and 1030 nm, and the beam intensities are achieved by beam defocusing. Since the determination of the welding mode or the welding mode transition during the welding process is a key factor for this investigation, the welding process is observed with *in-situ* x-ray phase contrast observation. Throughout the phase contrast difference between the presence of the keyhole and melt pool, the welding mode or its transition is distinguished. Furthermore, the influence of the limited material thickness on the vapor and melt dynamic is investigated in this paper when the melt or vapor penetrates the lower side of the material.

II. STATE OF THE ART

A. Observation using synchrotron phase contrast method

The ever deeper understanding of laser-based processes in metals demands ever newer diagnostic methods to understand and master the complex processes within the molten bath. In addition to the simple high-speed videography of the surface, more and more investigations of the processes inside the material with the help of x rays are being used. But here, too, development continues so that conventional x-ray sources such as those used in Refs. 3 and 4 are no longer sufficient in terms of spatial and temporal resolution. In order to increase the detail and resolution, more and more investigations with synchrotron radiation sources are the focus of research. This allows not only the higher resolutions already mentioned, but also the phase boundaries between solid/liquid and liquid/gas to be displayed in a new kind of quality.^{5–7}

In this paper, a monochromatic x-ray beam from the electron accelerator ring DESY in Hamburg with an energy of 37.7 keV and an average beam diameter of approximately 3 mm is used to screen the welded samples during the joining process. Local differences in density due to the aggregate state of the sample in the melting range lead to a weakening of the beam. This locally attenuated x-ray projection behind the sample was converted by the scintillator to visible light, which was recorded by the high-speed camera at a frame rate of 1000 fps, with a spatial resolution of 256 pixels/mm and an image size of 920 × 920 pixels, resulting in an exposed area of approximately 3 mm in diameter. Due to the small divergence of the x-ray beam between 0.0055 and 0.027 mrad, the impact of the penumbra on the observed blurring is negligible.

B. Heat conduction welding vs deep penetration welding

The heating or melting of metallic materials by means of laser radiation is based on the interaction between light and matter. This interaction is generally described by the absorption behavior of a certain material with a given surface characteristic, temperature, and wavelength as well as the polarization. When there is a simple interaction between the laser beam and the material, the material is heated. The degree of heating is determined by the energy balance of the workpiece, which is largely determined by the actual laser energy input, convection, and conduction of the workpiece.^{8,9}

If the laser beam exceeds a certain intensity, the heating leads to a local melting of the material on the surface at the contact point between the laser beam and the workpiece. Due to the changed state of aggregation of the material, both the absorption properties and the energetic balance of the system under consideration can change significantly. The characteristics of the melt and, thus, also of the resulting weld are largely determined by the heat conduction properties of the material. The resulting seam shape has an aspect ratio of ≈ 0.5 —quotient of seam width and welding depth—so that a semicircular seam cross section is created: The heat conduction weld.^{8–10}

With a further increase in intensity above a critical threshold, the melt created by the simple interaction begins to evaporate. The resulting vapor pressure creates a cavity in the melt pool, which, if

sufficiently formed, allows the reflected radiation to interact with the melt again. This causes the material to absorb the laser energy dramatically as each further interaction between the light and the matter leads to a deeper cavity—the keyhole—and the deeper the keyhole, the more interactions take place. In this deep penetration welding, the aspect ratio of the resulting weld geometry is ≈ 10 so that narrow deep welds are representative of this process variant.⁸

C. Welding using visible wavelength

When light meets material, it can interact in three different ways. On the one hand, the light can be absorbed, which leads to heating of the component. Furthermore, part of the light is reflected on the surface of the material. The third part transmits through the material, which can be neglected in the interaction with light and metallic materials if the material is sufficiently thick. The degree of absorption depends to a large extent on the surface properties, the component temperature, and the wavelength used. For copper-based alloys, this degree of absorption for wavelengths around 1 μm is approximately 5%. By reducing the wavelength when using green (515/530 nm) or blue (450 nm) laser sources, the absorption changes to 60%–70%. By using these beam sources with a higher absorption when processing copper-based alloys, it is possible to stabilize irregularities in the beam's absorption during the first singular interaction between light and matter.^{11–13}

D. Vapor pressure in the keyhole

The vapor capillary is generated by forces resulting from evaporation processes on the material surface and the resulting vapor flow. This evaporation process is necessary for laser deep penetration welding and influences the process flow. Thus, the outflowing metal vapor extracts energy from the process and enables the formation of a laser-induced plasma. Furthermore, the metal vapor flow causes shear stresses on the capillary wall, which partially causes the melt pool flow. The pressure distribution in the capillary, together with the alloy composition, determines the evaporation temperature on the capillary wall and, thus, influences the energy introduced into the workpiece, the temperature field and, thus, also the seam geometry.¹⁴

A stable capillary is created by the balance of forces between the vapor pressure in the capillary, which maintains the capillary and the forces of the surrounding melt that try to close the capillary. The resulting force from the recoil pressure of the evaporated material balances the forces from the surface tension and the hydrostatic pressure of the melt.¹⁵

III. EXPERIMENTAL SETUP AND IMAGE PROCESSING

A. Experimental setup

The experiments are conducted at the high energy beamline P07 (EH4) of Petra III at the Deutsches Elektronen-Synchrotron DESY in Hamburg for the laser beam spot welding of aluminum. The customized experimental setup for this investigation is based on the setup from Ref. 12, which is developed at the Chair of Laser Technology at RWTH Aachen University and the Fraunhofer Institute for Laser Technology ILT. This installed setup at beamline P07 (EH4) is shown schematically in Fig. 1.

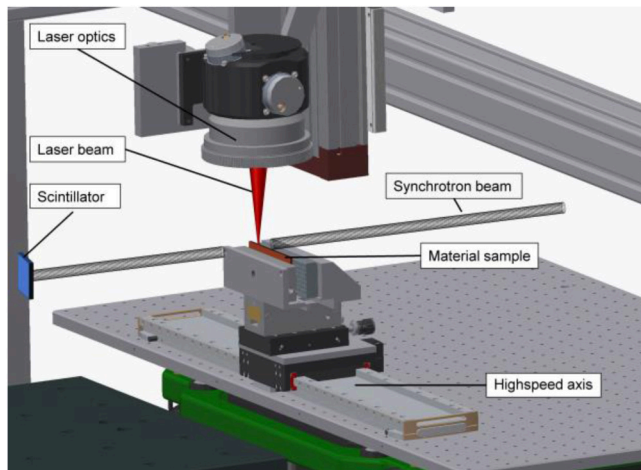


FIG. 1. Experimental setup for phase contrast observation of laser welds (CAD Model).

In this work, we have used an aluminum alloy 1050A ribbon with a dimension of $w \times l \times h = 3 \times 100 \times 0.5 \text{ mm}^3$, which is fixed on an aluminum plate. The laser beam spot welding process on the limited material thickness requires, however, a special preparation to observe the full penetration and related melt pool dynamics at the lower side of the specimen. Therefore, an adequate gap between the specimen and the base plate is foreseen for this experimental setup. If the gap is too narrow, the generated melt at the lower side of the specimen may bridge the gap and manipulate the experimental result. For the gap realization, grooves are milled vertically to the base plate with a depth of 2.5 mm and a width of 3 mm in 6 mm steps (Fig. 2). The pre-assembled aluminum plate is attached at the fixture mounted on an electromagnetic high-speed axis to place the specimen at the intersection of the laser and the synchrotron beam.

The scintillator with CdWO_4 (Cadmiumwolframat) is used to detect the synchrotron radiation and subsequently illuminates depending on the radiated intensity of the x-ray beam. The field area of the scintillator is $11 \times 11 \text{ mm}^2$ with a thickness of $300 \mu\text{m}$. The illuminating scintillator is filmed inside of an optical tower of

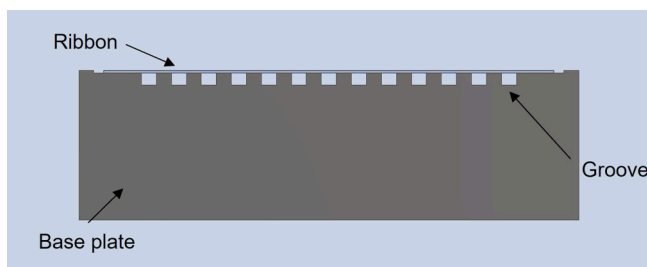


FIG. 2. Specimen used for the experiment.

TABLE I. Synchrotron setup and parameters for the investigation.

Parameter	Unit	P07 Petra 3
Operation mode	—	Low Beta
Photon energy	keV	37.7
Beam area	mm^2	2×2
Scintillator material	—	CdWO_4
Scintillator size	mm^2	11×11
Scintillator thickness	μm	300
Distance scintillator—material sample	mm	800

the beamline with optimum surrounding darkness from its back-side. A high-speed camera (Photron Fastcam SA5) is implemented inside the optical tower to record the keyhole and melt pool dynamic at a high frame rate of 1 kHz. The camera was set to 1024×768 pixels.

For the experiments, the following beamline parameters are used, as presented in Table I.

Two laser beam sources from Trumpf are used for this experiment: TruDisk 5001 and TruDisk 1020. The purpose of using two laser beam sources is to investigate the influence of absorptivity at comparable laser beam settings. The collimated laser beam is positioned at the specimen surface with a scanner from Newson with adequate coating for each laser beam wavelength. The following laser beam sources and optical setup are used as presented in Table II.

B. Image processing

The captured raw x-ray image of the illuminating scintillator requires a further image processing process to obtain a distinguishable phase difference inside of the irradiated specimen. Even though the intensity maximum of the radiation is directed to the melt pool and the vapor capillary, the captured gray-scale contrasts between both material phases are difficult to distinguish due to the superimposition by the beam shape. The main reasons are locally variable intensity of the synchrotron radiation and the temporal as well as local distribution of intensities of the beam.

TABLE II. Laser beam sources and optical setup used for the investigation.

Parameter	Unit	Trumpf TruDisk 1020	Trumpf TruDisk 5001
Wavelength	nm	515	1030
Laser power (max.)	W	1000	5000
Fiber diameter	μm	50	50
Focal length collimator	mm	100	80
Focal length optics	mm	70	163
Focal diameter	μm	81.0	117.3
(measured)			
Focal diameter +1 mm	μm	238	—
(measured)			
Focal diameter +2 mm	μm	494	—
(measured)			

The local and temporal perception of the gray-scale contrasts are, therefore, improved by correcting the intensity distribution based on the synchrotron beam shape. For this purpose, a recording of the synchrotron beam shape, hereinafter referred to as the *raw beam recording*, is made before each weld. This *raw beam recording* is then used to correct the recordings during the welding process, called *setup recording* in the following.

For this purpose, the arithmetic mean is calculated for each horizontal pixel line in the *raw beam recording* and *setup recording*. The mean value of the *setup recording* is then divided by the mean value of the *raw beam recording* to calculate a correction factor, which is used to increase the setup recording intensity to the level of the *raw beam recording*. By subtracting the *raw beam recordings* from the “corrected” *setup recording*, an image is then calculated in which the phase contrasts are more clearly emphasized. After the subtraction, the resulting gray levels are scaled up to 16 bit.

IV. RESULTS AND DISCUSSION

A. Observation of the laser-spot welding process on a limited material thickness

During the laser-spot welding process, a single position of the specimen is irradiated by the laser beam. Therefore, the development of the melt and keyhole over the process duration as well as the geometrical change of the specimen can be well observed. In Fig. 3, two x-ray phase contrast observation images are shown for interpretation while the laser-spot welding process is ongoing and after the solidification.

The x-ray image sequence of the laser-spot welding process of 0.5 mm thick Al1050A ribbon until the solidification of the melt is captured with the phase contrast method is shown in Fig. 4. The TruDisk 5001 is used for irradiation of $t = 50$ ms with $P = 500$ W at the focal position.

Based on the observation of the melt and keyhole evolution for the laser-spot welding process with a limited material thickness, this process can be divided into four different stages:

1. Progressive increase in the melt toward the lower side of the material with a deepened vapor capillary ($t < 10$ ms);

2. Formation of the “lens-like” melt at the lower side of the material and the vapor capillary reaches the lower side of the material ($t = 10$ ms);
3. Vapor capillary penetrates occasionally through the melt pool and causes the melt ejection ($24 \text{ ms} < t < 50 \text{ ms}$);
4. Solidification process of the melt ($50 \text{ ms} < t < 82 \text{ ms}$).

1. Stage 1

A $160 \mu\text{m}$ deep keyhole is observed 3 ms after the laser beam irradiation inside of the material, which is surrounded by the melt pool. As the irradiation continues, the depth of the keyhole increases and the melt volume increases as well. When the melt pool reaches the lower side of the material, the narrow end of the keyhole geometry changes into a round shape and forms an ellipsoid shaped vapor at $t = 9$ ms. The volume of the ellipsoid vapor is calculated with two measured semi-axis values ($a = 92 \mu\text{m}$, $b = 142 \mu\text{m}$) and one hypothetical semi-axis value ($c = a = 92 \mu\text{m}$), resulting in a volume of $V_{\text{vapor}_1030\text{nm}} = 5.03 \times 10^{-3} \text{ mm}^3$. The ellipsoid vapor induces a half ellipsoid vapor “lens-like” melt volume with $V_{\text{melt}_1030\text{nm}} = 4.3 \times 10^{-3} \text{ mm}^3$ ($a = 105 \mu\text{m}$, $b = 140 \mu\text{m}$, $c = b = 140 \mu\text{m}$). This expanded vapor capillary volume is more than factor 2 times larger than the keyhole volume ($V_{\text{keyhole}_1030\text{nm}} = 2.27 \times 10^{-3} \text{ mm}^3$) after the “lens-like” melt formation. The melt front is steady compared to the keyhole despite the sudden increase in the vapor capillary volume. Until $t = 9$ ms, no explicit melt formation at the lower side of the material is observed.

2. Stage 2

The “lens-like” melt at the lower side of the material is now clearly observed after the occurrence of an ellipsoid shaped vapor capillary ($t = 10$ ms). At the first appearance of the “lens-like” melt, the amplitude reaches its maximum value with $a = 204 \mu\text{m}$ and flat out over time. The keyhole shape has returned to the needle shape and maintains the keyhole diameter of $d = 76 \mu\text{m}$ until the end of the welding process. After the formation of the “lens-like” melt, the melt pool shape inside of material changes from a trapezoid with a segment of circle to rectangle ($t = 18$ ms). As the keyhole penetrates

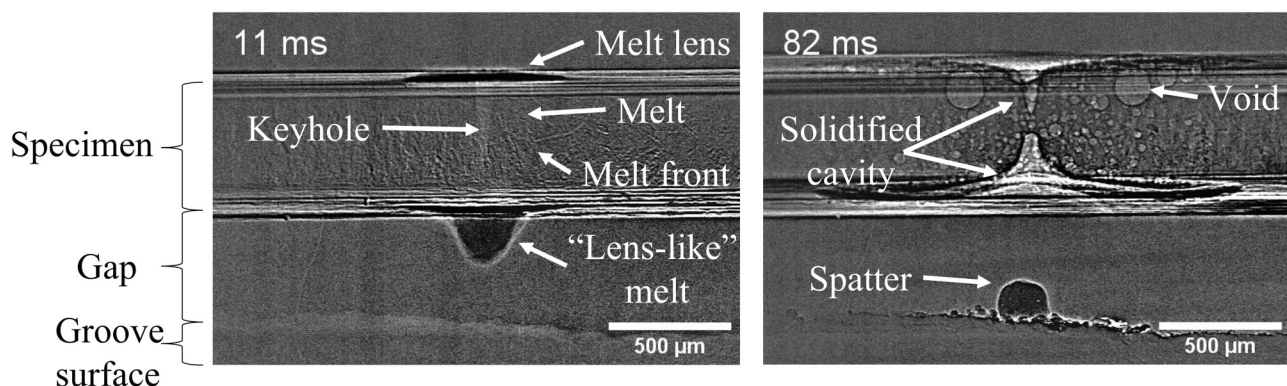


FIG. 3. Example x-ray phase contrast image of the interpretation during and after the laser-spot welding process.

through the material thickness but not through the “lens-like” melt, the melt pool diameter at the upper and lower side of the material becomes comparable. At the same time, the diameter of the “lens-like” melt also increases equally to the melt pool diameter at the lower side of the material. No sign of spatter ejection is observed until $t = 23$ ms.

3. Stage 3

The further laser beam irradiation leads to the melt pool enlargement. However, in exchange, the spatter ejections are observed due to the occasional laser beam penetration through the “lens-like” melt. Even for the laser beam penetration, the “lens-like” melt exists and expands continuously. The “lens-like” melt volume reaches up to $V = 0.009 \text{ mm}^3$ ($h = 0.41 \text{ mm}$, $a = 0.035 \text{ mm}$) at $t = 49$ ms, respectively. The solidified spatters are attached and gathered at the grooved surface. As the laser beam irradiation continues, more spatters are observed until the laser beam shut-off at $t = 50$ ms. The first visible trapped air in the melt pool is observed at $t = 34$ ms.

4. Stage 4

The laser beam is shut-off at $t = 50$ ms and the oscillation of the “lens-like” melt ends too. The trapped air during the welding process is clearly visible in the solidified melt and the fully solidified melt of the laser-spot welding is shown at the last image sequence ($t = 82$ ms). The solidification takes $t = 32$ ms based on the observation and a deep cone shaped cavity is observed after the solidification with $V = 0.02 \text{ mm}^3$ ($h = 0.32 \text{ mm}$, $r = 0.25 \text{ mm}$). The volume of the sphere-shaped spatter below the specimen is, however, only $V = 0.004 \text{ mm}^3$.

a. Influence of absorptivity. The influence of the absorptivity on the laser-spot welding process on the limited material thickness is investigated with the TruDisk 1020 with $\lambda = 515 \text{ nm}$. As the material Al1050A shows 5% higher laser beam absorptivity with $\lambda = 515 \text{ nm}$ compared to the laser beam with $\lambda = 1030 \text{ nm}$,¹⁶ the irradiated laser beam energy is reduced by shortening the irradiation time to $t = 20$ ms. The laser beam power is set equal to the welding experiment with near-infrared (NIR) laser beam source to perform a comparable laser beam intensity value. The x-ray phase contrast image sequence of the laser-spot welding process with $\lambda = 515 \text{ nm}$ is shown in Fig. 5.

The mentioned four stages of the laser-spot welding process are also observed with TruDisk 1020. As expected, the increased laser beam absorptivity leads to rapid keyhole penetration into the material where the spatter ejection occurs already at $t = 4$ ms. The expansion of the vapor capillary is also observed in this image sequence. During the welding process between $t = 6$ ms and $t = 8$ ms, the vapor capillary expands up to the melt front and consequently the melt pool is forced toward the outside of the material. The sphere cap shaped “lens-like” melt volume is $V_{\text{melt}, 515\text{nm}} = 0.021 \text{ mm}^3$ ($a = 0.24 \text{ mm}$, $h = 0.19 \text{ mm}$) and sphere-shaped vapor capillary volume is $V_{\text{vapor}, 515\text{nm}} = 0.0205 \text{ mm}^3$ ($r = 0.17 \text{ mm}$) at $t = 7$ ms, respectively. The vapor volume impacts the volume of the “lens-like” melt. Corresponding to the high dynamic of the vapor capillary, the resulting “lens-like” melt

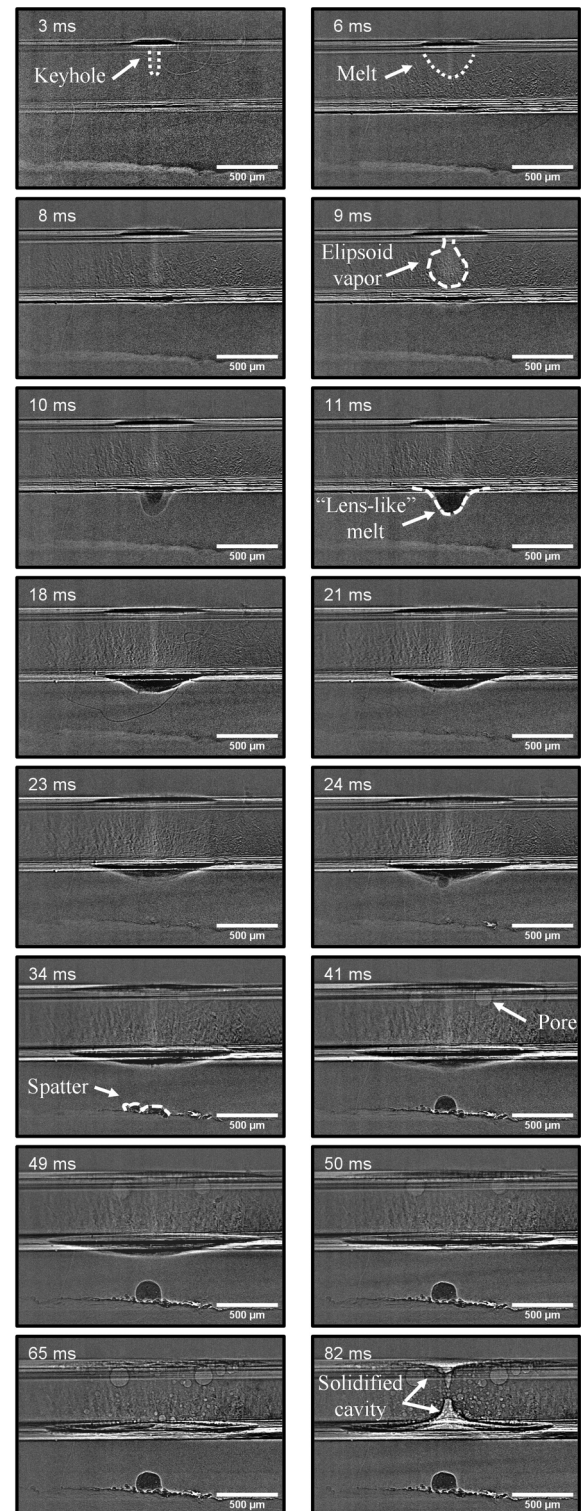


FIG. 4. Image sequence of laser-spot welding with 1030 nm.

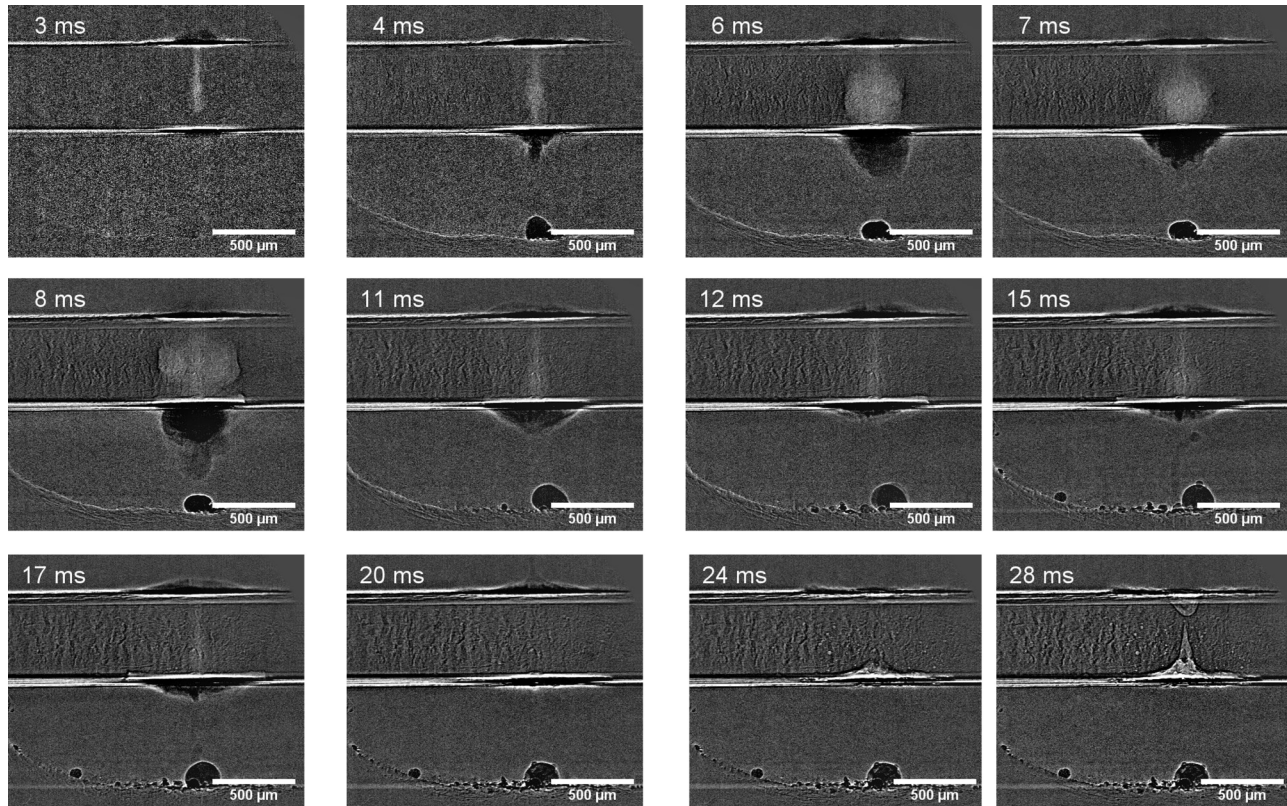


FIG. 5. Image sequence of laser-spot welding with 515 nm.

fluctuates dynamically and the increased volume of the “lens-like” melt is captured in this image sequence. As the vapor capillary returns to needle shape, the “lens-like” melt volume decreases and oscillates only with low amplitude until the laser beam is shut-off. The laser beam penetrates occasionally the “lens-like” melt and results in spatter ejection. The higher absorptivity of the laser beam leads to a faster pace of the temperature increase, which results in reduced beam irradiation time for the penetration of the limited material thickness. Therefore, the temperature gradient between the melt and surrounding material is higher than in the previous welding experiment with NIR laser beam leading to a faster

solidification process which ends already $t = 8$ ms after the laser beam shut-off. The solidified melt geometry is, however, comparable to the NIR weld result in Fig. 4 due to the fully penetrated keyhole during the welding process.

Based on the two image sequences (Figs. 4 and 5), the influence of the increased absorptivity can be summarized in terms of the laser-spot welding process on the limited material thickness:

- Reduced duration for the material penetration for TruDisk 1020 ($t = 6$ ms);
- High vapor capillary volume difference above the lower side of the material at the incidence of the “lens-like” melt generation ($V_{\text{vapor}_515\text{nm}}/V_{\text{vapor}_{1030\text{nm}}} \approx 4$);
- Increased volume of the “lens-like” melt corresponding to the size of the volume of the vapor capillary ($V_{\text{melt}_515\text{nm}}/V_{\text{melt}_{1030\text{nm}}} \approx 5$);
- Comparable ratio between vapor and “lens-like” melt for both laser beam source ($V_{\text{vapor}_{1030\text{nm}}}/V_{\text{melt}_{1030\text{nm}}} \approx 1.17$; $V_{\text{vapor}_515\text{nm}}/V_{\text{melt}_515\text{nm}} \approx 0.97$);
- Spatter ejection is not avoidable for both given settings.

b. Influence of the focal position. For both laser beam sources, a clear keyhole welding mode is observed at the focal length of the

TABLE III. Investigated values for varying focal position.

Focal position z (mm)	Beam diameter d_z (μm)	Ratio of beam diameter and material thickness (—)	Resulting intensity value with $P = 500$ W, I (MW/cm^2)
0	81	0.16	9.7
1	238	0.48	1.1
2	494	0.99	0.26

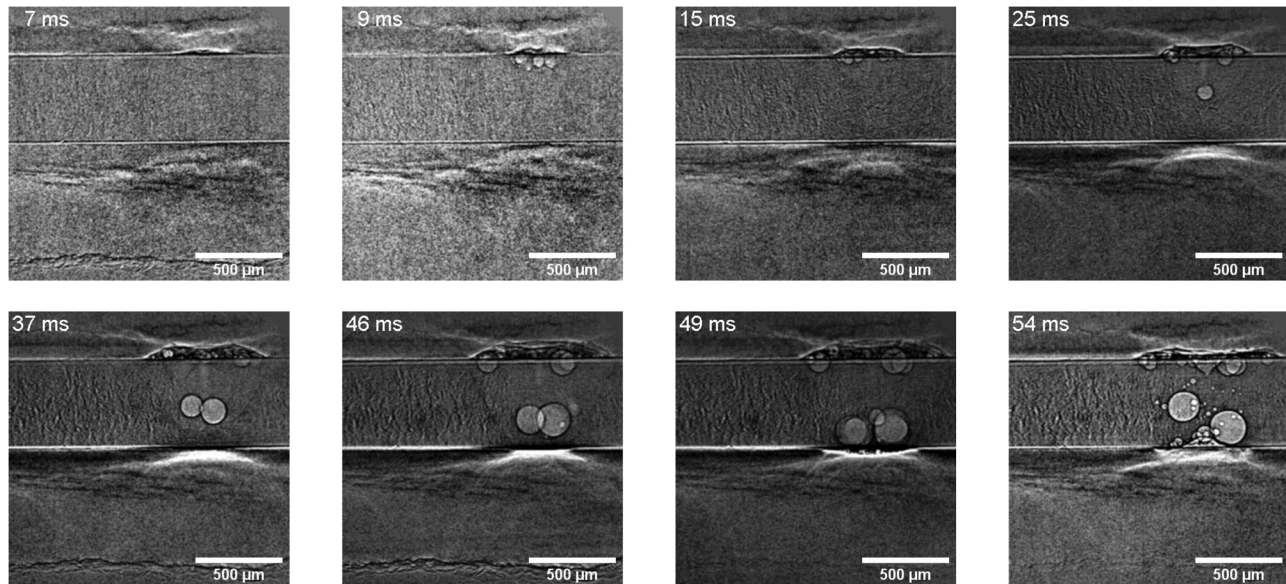


FIG. 6. Image sequence of laser-spot welding with 515 nm with focal position 1 mm offset in the z-axis.

laser beam. A transition from the heat conduction welding (HCW) to KW mode is, therefore, not observed as well. The behavior of the laser-spot welding process with the increasing ratio of the beam diameter to the material thickness (d_z/h) is carried out with a defocused laser beam on the specimen surface to observe the HCW. As the beam diameter varies, the resulting intensity value varies according to $I = (4 \cdot P/\pi \cdot d_z^2) (\text{MW}/\text{cm}^2)$. To guarantee sufficient laser beam energy despite the defocused laser beam, the laser beam source with a wavelength of 515 nm is applied for this investigation. The investigated values for the mentioned ratio are listed in Table III with their intensity values.

Besides the focal position, all laser beam parameters are equal to previous welding processes. The x-ray image sequence of each welding process with 1 mm focal offset is shown in Fig. 6.

Until $t = 15$ ms, the welding process is conducted with HCW mode different from the laser-spot welding process at the focal position. However, a clear void inside of the melt surface is

observed from $t = 9$ ms, which increases its volume as the welding process continues. A transition from HCW to KW keyhole occurs at $t = 15$ ms but the depth of the keyhole is limited to $132 \mu\text{m}$ until the end of the welding process. Despite the limited keyhole depth, the melt volume reaches the lower side of the specimen at $t = 46$ ms. A sign of a flat melt at the lower side of the specimen is to be observed at $t = 49$ ms. The thermal propagation due to the ratio of beam diameter and the material thickness or not efficient beam intensity may have influenced the behavior of the “lens-like” melt. The cavity of the solidified weld seam at the upper and lower sides of the specimen is yet present with $80 \mu\text{m}$ depth each. Different from the 1 mm focal offset welding result, the 2 mm focal offset welding process leads to pure HCW mode and the x-ray image sequence of each welding process with 2 mm focal offset is shown in Fig. 7.

With a given laser beam parameter, a full penetration of the material is not achieved, and a keyhole or mode transition is

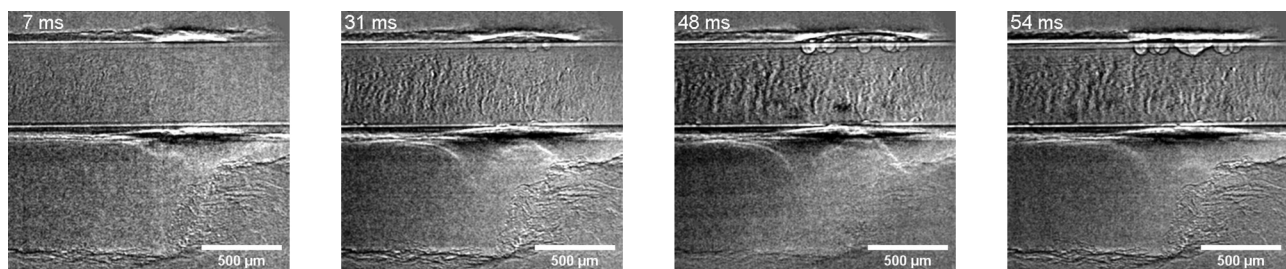


FIG. 7. Image sequence of laser-spot welding with 515 nm with focal position 2 mm offset in the z-axis.

observed at all. Therefore, a homogenous melt front development in a semicircular shape is observed until the end of the process. The reached melt depth is only $408\text{ }\mu\text{m}$, respectively. Equal to Fig. 5, voids at the melt surface are also observed during the HCW resulting that the presence of the keyhole is not responsible for the void formation at least for the upper side of the specimen. As the melt or keyhole penetrates the material, only a cavity at the upper side is observed with low depth.

V. CONCLUSION AND OUTLOOK

The x-ray phase contrast observation of the laser-spot welding process with a limited material thickness is investigated in this paper. To distinguish the phase contrast difference between the solid, liquid, and gas, the raw image recordings are further processed. The image processing is based on the arithmetic mean calculation for each horizontal pixel line in the raw beam and setup recording. The mean value of the setup image is then divided by the mean value of the raw beam image to calculate a correction factor, which raises the intensity of the setup image to the level of the raw beam images. By subtracting the raw beam images from the corrected setup image, an image is then calculated in which the phase contrasts are more clearly emphasized.

The *in-situ* laser-spot welding process of the limited material thickness can be divided into four stages from the keyhole formation until the melt solidification at a comparable laser beam intensity value independent of the applied laser beam source:

1. A progressive increase in the melt and keyhole;
2. Formation of the “lens-like” melt at the lower side of the material;
3. Full penetration of the vapor capillary and resulting in the melt ejection;
4. Solidification process of the melt.

The increased laser beam absorption leads to more absorbed energy in the specimen, which consequences in a rapid transition of defined stages due to the rapid keyhole development followed by 6 ms earlier full penetration compared to the experiment with the NIR laser beam source. Besides the rapid stage transition, the vapor volume at the “lens-like” melt formation shows strong absorptivity dependency. Due to the large vapor volume, a large “lens-like” melt is formed at the lower side of the specimen for the experiment with green wavelength. The measured vapor volume difference between laser beam sources is factor 4, whereas the measured “lens-like” melt volume difference is factor 5. The vapor and “lens-like” melt volumes are comparable for both used laser beam wavelength. Consequently, the vapor volume above the “lens-like” melt determines the volume of “lens-like” melt at the lower side of the specimen.

The variation of the beam diameter value at an equal energy input to the specimen leads to different welding modes. On the one hand, a welding mode transition from HCW to KW is observed when the focal position is defocused by 1 mm. However, the keyhole depth is only limited to $d = 132\text{ }\mu\text{m}$, respectively, until the laser beam shut-off. On the other hand, the outcome of the 2 mm defocusing of the laser beam position is only HCW without any keyhole formation.

As for the next step of the investigation, enhanced quality of the images is required for clear observations of contrast between each phase. For this purpose, a scintillator with another material is required for a higher photon energy of the x ray combined with a higher frame rate. Also, to increase the image quality thinner ribbon should be used for the experiment to ensure more transmission of x ray through the specimen.

Further investigation for this observation can proceed with the so-called “Laser Impulse Metal Bonding (LIMBO)” process where the “lens-like” melt is deflected toward the underlying joining partner to bridge the defined gap.¹⁷ Since the vapor volume influences the “lens-like” melt, further temporal or spatial beam modulation can be investigated to manipulate the vapor dynamic and consequently the “lens-like” melt shape and volume. Besides the melt and vapor dynamic, the occurrence of the trapped air is required to be investigated. Depending on the welding mode, the trapped air is visible in the melt and forms a void in the weld after the solidification. Also, the correlation between the fully penetrated keyhole during the welding process and solidified cone shaped cavity at the lower side of the solidified weld should be investigated.

ACKNOWLEDGMENTS

The presented investigations were carried out at RWTH Aachen University within the framework of the Collaborative Research Centre (No. SFB1120-236616214) “Bauteilpräzision durch Beherrschung von Schmelze und Erstarrung in Produktionsprozessen” and funded by the Deutsche Forschungsgemeinschaft e.V. (DFG, German Research Foundation). The sponsorship and support is gratefully acknowledged.

AUTHOR DECLARATIONS

Conflict of Interest

The authors have no conflicts to disclose.

Author Contributions

Woo-Sik Chung: Conceptualization (equal); Investigation (lead); Methodology (equal); Writing – original draft (lead); Writing – review & editing (equal). **André Häusler:** Writing – original draft (equal). **Marc Hummel:** Conceptualization (equal); Project administration (lead). **Alexander Olowinsky:** Supervision (equal); Writing – review & editing (lead). **Arnold Gillner:** Supervision (equal). **Felix Beckmann:** Data curation (equal). **Julian Moosmann:** Data curation (equal).

REFERENCES

- ¹S. S. Lee, T. H. Kim, S. J. Hu, and W. W. Cai, “Joining technologies for automotive lithium-ion battery manufacturing, American Society of Mechanical Engineers,” in *ASME International Manufacturing Science and Engineering Conference 2010*, Erie, Pennsylvania, 12–15 October 2010 (ASME, New York, 2018).
- ²P. Heinen, A. Häusler, B. Mehlmann, and A. Olowinsky, “Laser beam micro-welding of lithium-ion battery cells with copper connectors for electrical connections in energy storage devices,” *Laser Eng.* **36**, 147–167 (2017).
- ³M. Miyagi, Y. Kawahito, H. Wang, H. Kawakami, T. Shoubu, and M. Tsukamoto, “X-ray phase contrast observation of solidification and hot crack propagation in laser spot welding of aluminum alloy,” *Opt. Express* **26**, 22626–22636 (2018).

- ⁴F. Fetzter, M. Boley, R. Weber, and T. Graf, "Comprehensive analysis of the capillary depth in deep penetration laser welding," *Proc. SPIE* **10097**, 1009709 (2017).
- ⁵J. Wagner, C. Hagenlocher, M. Hummel, A. Olowinsky, R. Weber, and T. Graf, "Synchrotron X-ray analysis of the influence of the magnesium content on the absorptance during full-penetration laser welding of aluminum," *Metals* **11**, 797 (2021).
- ⁶J. Lind, C. Hagenlocher, D. Blazquez-Sanchez, M. Hummel, A. Olowinsky, R. Weber, and T. Graf, "Influence of the laser cutting front geometry on the striation formation analysed with high-speed synchrotron X-ray imaging," *IOP Conf. Ser.: Mater. Sci. Eng.* **1135**, 012009 (2021).
- ⁷M. Hummel, A. Häusler, S. Hollatz, C. Hagenlocher, J. Lind, U. Halm, and A. Gillner, "Temporally and spatially highly resolved reconstruction of vapor capillary geometry during laser beam welding using synchrotron radiation," in *Lasers in Manufacturing Conference 2021, Munich, Germany, 21–24 June 2021* (Wissenschaftliche Gesellschaft für Lasertechnik e.V., RWTH Aachen, Aachen, 2022).
- ⁸H. Hügel and T. Graf, *Laser in der Fertigung. Strahlquellen, Systeme, Fertigungsverfahren, 2. neu bearb. Aufl.* (Vieweg+Teubner, Wiesbaden, 2022) (Aus dem Programm Fertigung).
- ⁹A. Heß, "Vorteile und Herausforderungen Beim Laserstrahlschweißen mit Strahlquellen Höchster Fokussierbarkeit," Dissertation, Herbert Utz Verlag, IFSW, Stuttgart, 2012.
- ¹⁰Reinhart Poprawe, *Lasertechnik für die Fertigung. Grundlagen, Perspektiven und Beispiele für den Innovativen Ingenieur; mit 26 Tabellen* (Springer, Berlin, 2005), pp. 257–259 (VDIBuch).
- ¹¹F. Kaufmann, J. Ermer, A. Maier, S. Roth, and M. Schmidt, "Influence of plume attenuation under high power laser welding of copper using visible wavelengths," *J. Laser Appl.* **33**, 042006 (2021).
- ¹²M. Hummel, M. Kulkens, C. Schöler, W. Schulz, and A. Gillner, "In situ X-ray tomography investigations on laser welding of copper with 515 and 1030 nm laser beam sources," *J. Manuf. Processes* **67**, 170–176 (2021).
- ¹³A. Heider, A. Hess, R. Weber, and T. Graf, "Stabilized copper welding by using power modulated green and IR laser beams," *ICALEO* **2011**, 395–402 (2011).
- ¹⁴P. Berger and H. Hügel, "Fluid dynamic effects in keyhole welding—An attempt to characterize different regimes," *Phys. Procedia* **41**, 216–224 (2013).
- ¹⁵R. Fabbro and K. Chouf, "Dynamical description of the keyhole in deep penetration laser welding," *J. Laser Appl.* **12**, 142–148 (2000).
- ¹⁶M. Hummel, A. Häusler, A. Olowinsky, A. Gillner, and R. Poprawe, "Comparing 1070 nm and 515 nm wavelength laser beam sources in terms of efficiency for laser microwelding copper," *Lasers Eng.* **46**, 187–202 (2020).
- ¹⁷W. Chung, A. Häusler, A. Olowinsky, A. Gillner, and R. Poprawe, "Investigation to increase the welding joint area with modulated laser beam welding over gap," *J. Laser Micro/Nanoeng.* **13**, 117–125 (2018).